phocyte proliferations observed in these patients. *LMO2* targeting suggests either that there is a "physical hotspot" of integration at this locus, or more likely, that random, activating, *LMO2* integrants are selected simply by the growth advantage conferred on them. The chance of integration of any active gene is assumed to be $\sim 1 \times 10^{-5}$ (a rough estimate of a random hit within 10 kbp among the estimated transcriptionally active 1×10^9 base pairs. It is likely that each patient received at least 1 to 10 *LMO2*-targeted cells, because the patients received 1×10^6 or more transduced T lymphocyte precursors (estimating that at least 1% of the total number of injected transduced cells—92×10^6 and 133×10^6 for patients P4 and P5, respectively—could give rise to T cells). It will be crucial to understand the site distribution and mechanism of retroviral integration in human CD34 cells in order to more accurately assess this risk. The availability of the human genome sequence makes this work feasible (*38, 39*). It is tempting to speculate that SCID-X1–related features may have contributed to the unexpectedly high rate of leukemia-like syndrome. Indeed, it is possible that, because of the differentiation block, there are more T lymphocyte precursors among CD34 cells in SCID-X1 marrow than in marrow of normal controls, thus augmenting the number of cells at risk for vector integration and further proliferation once the γc transgene is expressed. The massive capacity of T cell precursors to become amplified in an "empty compartment" is another possible factor that favors the development of disease (*40*). Finally, patients P4 and P5 were the youngest in our study. Given the exceptional proliferative capacity of neonatal hematopoiesis, young age per se could also increase the number of precursor cells at risk

for insertional mutagenesis. These hypotheses can now be tested by the design of predictive model(s) that enable assessment of the safety of modified gene therapy strategies that should be envisaged to treat SCID-X1 patients, as justified by the efficacy of gene therapy observed in this trial. Our observations demonstrate that the safety profile of each gene transfer strategy needs to be addressed individually for each disease in relation to its pathophysiology and the functions of the transgene product.

References and Notes
1. M. Cavazzana-Calvo *et al.*, *Science* **288**, 669 (2000).
2. S. Hacein-Bey-Abina *et al.*, *N. Engl. J. Med.* **346**, 1185 (2002).
3. A. Aiuti *et al.*, *Science* **296**, 2410 (2002).
4. S. Hacein-Bey *et al.*, *Blood* **87**, 3108 (1996).
5. M. Schmidt *et al.*, *Blood* **100**, 2737 (2002).
6. M. Schmidt *et al.*, in preparation.
7. Z. Li *et al.*, *Science* **296**, 497 (2002).
8. S. Hacein-Bey-Abina *et al.*, *N. Engl. J. Med.* **348**, 255 (2003).
9. X. Lafarge *et al.*, *J. Infect. Dis.* **184**, 533 (2001).
10. W. A. Kamps *et al.*, *Blood* **94**, 1226 (1999).
11. C. Pannetier *et al.*, *Proc. Natl. Acad. Sci. U.S.A.* **90**, 4319 (1993).
12. J. Dechanet *et al.*, *J. Clin. Invest.* **103**, 1437 (1999).
13. A. Lim *et al.*, *J. Immunol. Methods* **261**, 177 (2002).
14. Materials and methods are available as supporting material on *Science* Online.
15. Immunofluorescence study revealed that P4 and P5 blast cells were positive for CD3, CD7, CD5, CD28, CD45RO, γc, and CD8 (for P5) and negative for CD4, CD1, CD10, CD34, CD19, CD56, and CD14.
16. R. E. Donahue *et al.*, *J. Exp. Med.* **176**, 1125 (1992).
17. E. F. Vanin, M. Kaloss, C. Broscius, A. W. Nienhuis, *J. Virol.* **68**, 4241 (1994).
18. M. Printz *et al.*, *Gene Ther.* **2**, 143 (1995).
19. X. Song *et al.*, *Proc. Natl. Acad. Sci. U.S.A.* **99**, 6269 (2002).
20. T. Boehm, L. Foroni, Y. Kaneko, M. F. Perutz, T. H. Rabbitts, *Proc. Natl. Acad. Sci. U.S.A.* **88**, 4367 (1991).
21. A. J. Warren *et al.*, *Cell* **78**, 45 (1994).
22. Y. Yamada *et al.*, *Proc. Natl. Acad. Sci. U.S.A.* **95**, 3890 (1998).
23. T. H. Rabbitts, *Oncogene* **20**, 5763 (2001).
24. V. E. Valge-Archer *et al.*, *Proc. Natl. Acad. Sci. U.S.A.* **91**, 8617 (1994).
25. I. Wadman *et al.*, *EMBO J.* **13**, 4831 (1994).
26. I. A. Wadman *et al.*, *EMBO J.* **16**, 3145 (1997).
27. B. Royer-Pokora, U. Loos, W. D. Ludwig, *Oncogene* **6**, 1887 (1991).
28. I. S. Garcia *et al.*, *Oncogene* **6**, 577 (1991).
29. P. Fisch *et al.*, *Oncogene* **7**, 2389 (1992).
30. R. C. Larson *et al.*, *Oncogene* **9**, 3675 (1994).
31. G. A. Neale, J. E. Rehg, R. M. Goorha, *Blood* **86**, 3060 (1995).
32. G. A. Neale, J. E. Rehg, R. M. Goorha, *Leukemia* **11**, 289 (1997).
33. K. Sugamura *et al.*, *Adv. Immunol.* **59**, 225 (1995).
34. O. Lantz, I. Grandjean, P. Matzinger, J. P. Di Santo, *Nature Immunol.* **1**, 54 (2000).
35. J. I. Cohen, unpublished data.
36. A. Aurias, unpublished data.
37. H. Mori *et al.*, *Proc. Natl. Acad. Sci. U.S.A.* **99**, 8242 (2002).
38. A. R. Schroder *et al.*, *Cell* **110**, 521 (2002).
39. X. Wu, Y. Li, B. Crise, S. M. Burgess, *Science* **300**, 1749 (2003).
40. A. A. Freitas, B. Rocha, *Annu. Rev. Immunol.* **18**, 83 (2000).
41. We are indebted to the families of the patients for their continuous support; to the medical and nursing staff of the Unité d'Immunologie et d'Hématologie Pédiatriques, Hôpital des Enfants Malades, for patient care; to F. Calvo, A. O. Cavazzana, D. Papadopoulo, P. Kourilsky, H. Bruzzoni-Giovanelli, C. Thibaut, P. Kastner, M. Bonneville, H. Vié, E. Vivier, and P. Paule for their contribution to the study; and to C. Hue for technical help. Supported by grants from INSERM; the Bundesministerium für Bildung, Wissenschaft, Forschung und Technologie; Deutsche Forschung Gemeinschaft; the Association Française contre les Myopathies; the Programme Hospitalier de Recherche Clinique of the Health Ministry (France); Assistance Publique–Hôpitaux de Paris; European Community contract no. QLK3-CT 2001 (G. Wagemaker, coordinator); and the Jeffrey Modell Foundation.

REPORTS

A Hybridization Model for the Plasmon Response of Complex Nanostructures

E. Prodan,[1] C. Radloff,[2] N. J. Halas,[2,3]* P. Nordlander[1,3]

We present a simple and intuitive picture, an electromagnetic analog of molecular orbital theory, that describes the plasmon response of complex nanostructures of arbitrary shape. Our model can be understood as the interaction or "hybridization" of elementary plasmons supported by nanostructures of elementary geometries. As an example, the approach is applied to the important case of a four-layer concentric nanoshell, where the hybridization of the plasmons of the inner and outer nanoshells determines the resonant frequencies of the multilayer nanostructure.

The fabrication of materials on a nanoscale can be used to enhance and exploit properties that become stronger under conditions of reduced dimensionality. In metallic systems, the conduction electron charge density and its corresponding electromagnetic field can undergo plasmon oscillations. Because of the nature of the optical constants for noble metals, the charge oscillations can propagate along the surface (rather than vanish evanescently) at optical frequencies. These surface plasmons can be excited by incident light in a process that depends on the dielectric constant of the material at the metal's surface, an effect that is exploited in surface plasmon resonance spectroscopy. In particles of dimensions on the order of the plasmon resonance wavelength, this surface plasmon dominates the electromagnetic response of the structure.

Recent advancements in the chemical synthesis of metal nanostructures have led to a proliferation of various shapes such as

[1]Department of Physics, [2]Department of Chemistry, [3]Department of Electrical and Computer Engineering, and the Rice Quantum Institute, Rice University, Houston, TX 77251, USA.

*To whom correspondence should be addressed. E-mail: halas@rice.edu

rods (*1*, *2*), shells (*3–5*), cups (*6*, *7*), rings (*8*), disks (*9*, *10*), and cubes. These developments, in addition to deep submicrometer lithographic methods for fabricating nanostructure grids and arrays, have provided the tools for realizing experimental studies of plasmon properties of metal nanostructures of arbitrary geometry. To fully exploit these new fabrication capabilities, accurate numerical methods (*11–13*) for calculating the electromagnetic properties of nanoscale structures are essentially defining the new field of "plasmonics," providing an understanding of how to manipulate light at the nanometer scale with metal nanostructures as nano-optical components.

We now describe a way in which the plasmon response of metal-based nanostructures can be understood as the interaction or "hybridization" of plasmons supported by metallic nanostructures of more elementary shapes. The plasmon hybridization picture can be used to describe the sensitive structural tunability of the plasmon resonance frequency of the nanoshell geometry as the interaction between plasmons supported by a nanoscale sphere and cavity (*14*). This simple and intuitive picture can also be used to understand the plasmon resonance behavior of composite metallic nanostructures of greater geometrical complexity. The plasmon hybridization picture is important because it provides the nanoscientist with a powerful and general design principle that can be applied, both qualitatively and quantitatively, to guide the design of metallic nanostructures and predict their resonant properties.

A hollow metallic nanosphere, or nanoshell, supports plasmon resonances with frequencies that are a sensitive function of the inner and outer radius of the metallic shell (*15*). Recent experimental realization of this topology by a variety of methods has demonstrated the sensitive dependence of the plasmon resonance frequency on nanostructure geometry and embedding medium (*3*, *16–19*). Although this property can be calculated with electromagnetic theory, it has also recently been shown that ab initio electronic structure methods result in exact agreement with Mie scattering theory (*20*) for nanoshells in the dipole limit (*21*). This convergence between electronic and electromagnetic theory for predicting the plasmon response of metal nanostructures provides the rigorous foundation for the plasmon hybridization picture.

For the specific case of nanoshells, the highly geometry-dependent plasmon response can be seen as an interaction between the essentially fixed-frequency plasmon response of a nanosphere and that of a nanocavity (Fig. 1). The sphere and cavity plasmons are electromagnetic excitations that in-
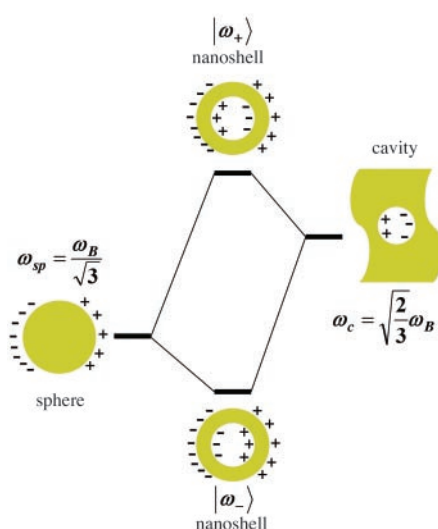
duce surface charges at the inner and outer interfaces of the metal shell. Because of the finite thickness of the shell layer, the sphere and cavity plasmons interact with each other. The strength of the interaction between the sphere and cavity plasmons is controlled by the thickness of the metal shell layer. This interaction results in the splitting of the plasmon resonances into two new resonances: the lower energy symmetric or "bonding" plasmon and the higher energy antisymmetric or "antibonding" plasmon (Fig. 1). To describe the geometry of a nanoshell, we adopt the notation (*a*,*b*) to indicate the inner radius *a* and the outer radius *b* of the shell.

The electron gas deformations can be decomposed as spherical harmonics of order *l*. We can show (supporting online text) that the interaction of the plasmons on the inner and outer surfaces of the shell gives rise to two hybridized plasmon modes $|\omega_+\rangle$ and $|\omega_-\rangle$ for each $l > 0$. The frequencies of these modes are

$$\omega_{l\pm}^2 = \frac{\omega_B^2}{2}\left[1 \pm \frac{1}{2l+1}\sqrt{1 + 4l(l+1)\left(\frac{a}{b}\right)^{2l+1}}\right]$$

(1)

The $|\omega_+\rangle$ mode corresponds to antisymmetric coupling between the sphere and cavity modes and the $|\omega_-\rangle$ mode corresponds to symmetric coupling between the two modes (Fig. 1). The validity of this expression for the nanoshell plasmon energies has been explicitly verified with fully quantum mechanical calculations (*20*). The inclusion of a dielectric core and/or embedding medium in the formalism is straightforward. Although
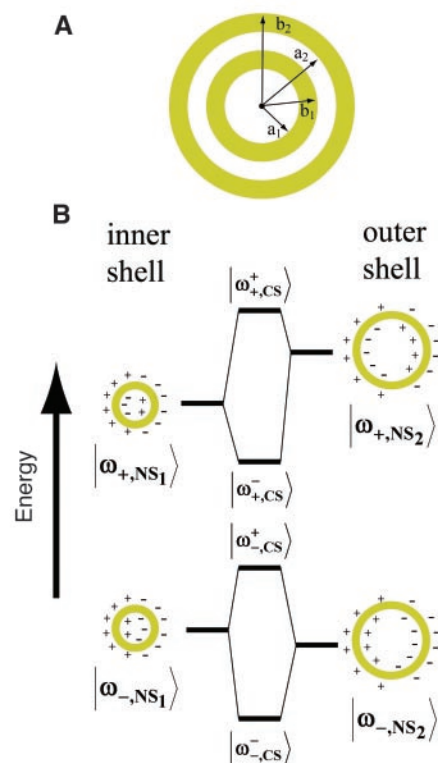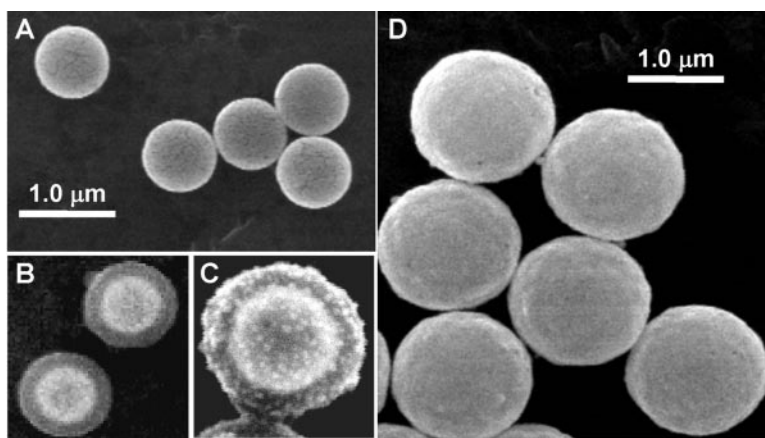

Fig. 1. An energy-level diagram describing the plasmon hybridization in metal nanoshells resulting from the interaction between the sphere and cavity plasmons. The two nanoshell plasmons are an antisymmetrically coupled (antibonding) ω_+ plasmon mode and a symmetrically coupled (bonding) ω_- plasmon mode.

Fig. 2. Diagrams depicting (**A**) the concentric nanoshell geometry described by the concentric radii of the core (a_1), inner shell (b_1), spacer layer (a_2), and outer shell (b_2). (**B**) An energy-level diagram describing the interaction between the inner- and outer-nanoshell plasmon resonances, resulting in the hybrid plasmon resonance of a concentric nanoshell. Although in principle, a coupling also exists between the antisymmetric and the symmetric nanoshell plasmons of the separate shells, it has only a small influence because of the larger energy separation between those two modes.

the resulting plasmon energies are the same as what would be obtained from a Drude dielectric function and classical Mie scattering in the dipole limit, the present treatment clearly elucidates the nature of the nanoshell plasmon resonances and, in particular, the microscopic origin of their tunability.

The plasmon hybridization picture can be used to understand the multifeatured plasmon response of more complex metallic nanostructures, such as dimers or other nanoparticle aggregates. The structure that we examine here is that of a concentric nanoshell, a four-layer nanoparticle consisting of a dielectric core, metal shell, dielectric spacer layer, and a second metallic shell. This "nano-matryushka" structure is shown in Fig. 2A. The plasmon response of this structure can be understood as an interaction and hybridization of the plasmons of the two individual metal shells (supporting online text). To illustrate this concept, we consider two concentric nanoshells with geometries (a_1,b_1) and

Fig. 3. Scanning electron micrographs depicting the synthesis of concentric nanoshells. (**A**) Silica nanoparticles were prepared with the Stöber method. The silica-particle surfaces were then derivatized with 3-aminopropyltriethoxysilane (APTES). This presents an amine moiety–coated nanoparticle surface for attaching small gold colloid (2- to 3-nm diameter). The attached gold colloid acts as nucleation sites for the reduction of gold ions from solution onto the particle. Once prepared, the nanoshells were processed to remove excess reactants by centrifugation and dialysis. Gold-silica nanoshells of 800 nm total diameter are shown. (**B**) The silica-encapsulated nanoshell with a 235-nm-thick silica layer. The growth of the silica layer onto the gold-silica nanoshell was achieved with a method similar to that developed for the silica encapsulation of gold colloid (23). The gold surface of the nanoshell was first derivatized with APTES. This treatment prepared the particles for the subsequent condensation of a thin (4 to 10 nm) silica layer onto their surfaces from a dilute (0.54 weight %) sodium silicate solution. Upon formation of this thin silica layer, centrifugation was used to remove excess silica from solution that may have nucleated into silica nanoparticles. The thickness of this silica layer was then increased by using the Stöber method (24). Growth of the outermost gold shell layer onto the silica layer proceeded by derivatization of the silica layer with APTES, attachment of small gold colloid, followed by reduction of the final gold shell layer. (**C**) The silica-coated nanoshell seeded with Au-colloid to initiate the growth of a second gold layer. The gold colloid coverage is comparable to the coverage typical of metal shell growth. Reduction of chloroauric acid onto this prepared nanoparticle yields the final four-layer, concentric nanoshell. (**D**) The completed concentric nanoshell with a total particle diameter of 1.4 μm.

Fig. 4. Experimental (blue) and theoretical (red) extinction spectra for concentric nanoshells (3) compared to the inner (1) and outer (2) nanoshell plasmon resonances in different-strength coupling regimes. Nanostructures were derivatized with 1-dodecanethiol and either suspended in CS_2 in a 1-mm path length sealed cell or dried and mixed with KBr and pressed into a pellet to obtain the spectra. The peak positions of the dipole resonance modes are marked for clarity. The theoretical extinction spectra were generated with a vector basis function solution of Mie scattering theory for a coated sphere. The inner-nanoshell spectra (1) were measured in solution before the growth of the a_2 and b_2 layers. (**A**) Concentric nanoshell with dimensions $a_1/b_1/a_2/b_2 = 80/107/135/157$ (nm); the inner- and outer-nanoshell plasmons interact strongly, resulting in strongly hybridized plasmons. (**B**) Concentric nanoshell with dimensions $a_1/b_1/a_2/b_2 = 77/102/141/145$ (nm); the inner- and outer-nanoshell plasmons interact weakly with a relatively small change in the concentric nanoshell plasmon compared with the single nanoshell plasmons. (**C**) Concentric nanoshell with dimensions $a_1/b_1/a_2/b_2 = 396/418/654/693$ (nm). Noninteracting inner- and outer-shell plasmons: The concentric nanoshell response is identical to that of the outer-nanoshell plasmon.
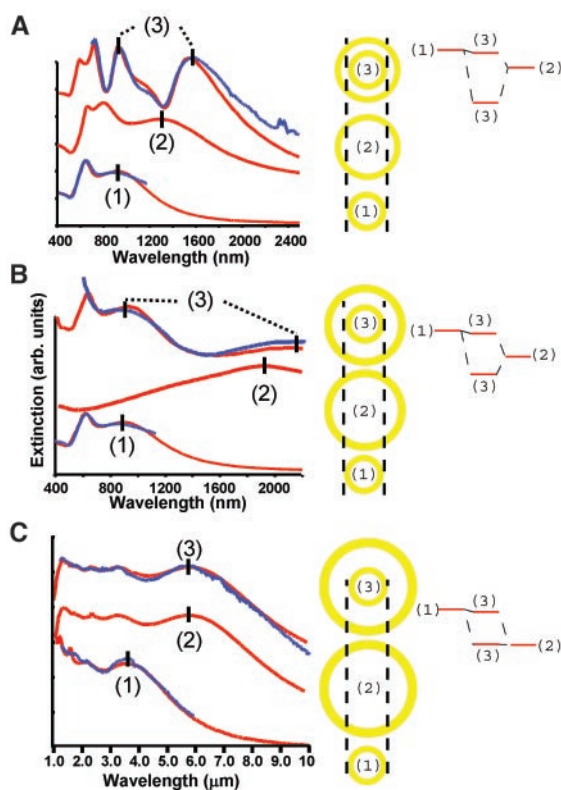
(a_2,b_2). In this system, there are four linearly independent, incompressible charge deformations (plasmons). Their interaction results in four hybridized plasmon resonances, as schematically depicted in Fig. 2B. The thickness of the dielectric spacer layer $|a_2 - b_1|$ controls the strength of the coupling between the inner and the outer nanoshell. The resulting plasmon energy shifts will depend on the coupling strength and the energy between the plasmons on the inner and outer shell. The plasmon energies of the concentric nanoshell structure can therefore be tuned both by changing the dielectric spacer layer and by tuning the plasmon energies of the individual nanoshells.

Concentric nanoshells were synthesized on the basis of the gold nanoshell fabrication chemistry previously reported (Fig. 3) (3). Figure 4 shows the hybridized plasmon response of concentric nanoshells for the cases of strong coupling (Fig. 4A), weak coupling (Fig. 4B), and uncoupled plasmons (Fig. 4C). In this figure, the spectra denoted (1) show the experimental and theoretical extinction spectra for the isolated inner-shell plasmon $|\omega_{-,NS_1}\rangle$. The spectra denoted (2) are the theoretical extinction spectra of the isolated outer-shell plasmon $|\omega_{-,NS_2}\rangle$, calculated as though the inner-shell structure were replaced wholly by a dielectric (silica) core. The spectra denoted (3) are the experimental and theoretical extinction for the concentric nanoshell. In these spectra, the $|\omega_{-,CS}^+\rangle$ and $|\omega_{-,CS}^-\rangle$ plasmons are clearly apparent.

In Fig. 4A, the strong coupling case, the plasmon hybridization and splittings are quite strong because of the small (28 nm) interlayer spacing between inner– and outer–metal shell layers and because the inner $|\omega_{-,NS_1}\rangle$ and outer $|\omega_{-,NS_2}\rangle$ nanoshell plasmons are nearly resonant with each other. The hybridization of the plasmon appears to be strongly asymmetric; we attribute this asymmetry primarily to phase-retardation effects (22). A second contributing factor to the asymmetry is the small but finite interaction with the higher energy $|\omega_{+,NS_1}\rangle$ and $|\omega_{+,NS_2}\rangle$ plasmon modes. Figure 4B depicts a concentric nanoshell with a weak plasmon coupling between the inner and outer shell. In this case, the inner- and outer-plasmon resonances are detuned from each other in energy, and the spacing between inner and outer metal layers is slightly increased (39 nm). Because the hybridization is weak, the concentric shell plasmon modes show only small shifts relative to the isolated shell plasmons. In Fig. 4C, a concentric nanoshell with a fully decoupled plasmon response is shown. In this case, the intershell spacing is 236 nm, effectively

isolating the inner-shell and outer-shell layers. The concentric nanoshell response (3) appears to be almost indistinguishable from the calculated nanoshell response for the outer shell. Because of the large intershell spacing and the finite penetration depth of the light, the inner-nanoshell plasmon is not excited.

We have shown that the plasmon response of metal-based nanostructures can be viewed as the collection of plasmons arising from simpler geometries to form an interacting system. The plasmonics of the metallic nanostructure is determined by the electromagnetic interaction between these "free" plasmons, which leads to mixing (hybridization), splittings, and shifts of the plasmon energies.

References and Notes

1. N. R. Jana, L. Gearheart, C. J. Murphy, *J. Phys. Chem. B*. **105**, 4065 (2001).
2. S. R. Nicewarner-Pena *et al.*, *Science* **294**, 137 (2001).
3. S. J. Oldenburg, R. D. Averitt, S. Westcott, N. J. Halas, *Chem. Phys. Lett.* **288**, 243 (1998).
4. C. Graf, A. van Blaaderen, *Langmuir* **18**, 524 (2002).
5. Y. Kobayashi, V. Salgueirina-Maceira, L. M. Liz-Marzan, *Chem. Mater.* **13**, 1630 (2001).
6. J. C. Love, B. D. Gates, D. B. Wolfe, K. E. Paul, G. M. Whitesides, *Nano Lett.* **2**, 891 (2002).
7. C. Charnay *et al.*, *J. Phys. Chem. B* **107**, 7327 (2003).
8. J. Aizpurua *et al.*, *Phys. Rev. Lett.* **90**, 057401 (2003).
9. M. Maillard, S. Giorgio, M. P. Pileni, *J. Phys. Chem. B.* **107**, 2466 (2003).
10. Y. Sun, Y. Xia, *Science* **298**, 2176 (2002).
11. K. L. Kelly, C. Eduardo, L. L. Zhao, G. C. Schatz, *J. Phys. Chem. B* **107**, 668 (2003).
12. S. A. Maier, M. L. Brongersma, P. G. Kik, H. A. Atwater, *Phys. Rev. B* **65**, 193408 (2002).
13. E. Prodan, P. Nordlander, *Chem. Phys. Lett.* **352**, 140 (2002).
14. E. Prodan, A. Lee, P. Nordlander, *Chem. Phys. Lett.* **360**, 325 (2002).
15. A. L. Aden, M. Kerker, *J. Appl. Phys.* **22**, 1242 (1951).
16. J. B. Jackson, N. J. Halas, *J. Phys. Chem. B* **105**, 2743 (2001).
17. M. D. Malinsky, K. L. Kelly, G. C. Schatz, R. P. Van Duyne, *J. Am. Chem. Soc.* **123**, 1471 (2001).
18. Y. Sun, Y. Xia, *Anal. Chem.* **74**, 5297 (2002).
19. S. L. Westcott, R. D. Averitt, J. A. Wolfgang, P. Nordlander, N. J. Halas, *J. Phys. Chem. B* **105**, 9913 (2001).
20. E. Prodan, P. Nordlander, *Nano Lett.* **3**, 543 (2003).
21. The dipole limit is the size range where the nanoparticle is small in comparison to the wavelength of light, such that the electromagnetic field across the extent of the nanoparticle can be assumed to be uniform. In this limit, retardation effects of the electromagnetic fields can be neglected, and the electromagnetic interactions can be described by the electrostatic limit of Maxwell's equations.
22. In the dipole limit (*21*), the interaction results in plasmon modes that repel each other, i.e., a symmetric splitting.
23. L. M. Liz-Marzan, M. Giersig, P. Mulvaney, *Langmuir* **12**, 43229 (1996).
24. W. Stöber, A. Fink, E. Bohn, *J. Colloid Interface Sci.* **26**, 62 (1968).
25. We acknowledge the Robert A. Welch Foundation (grants C-1220 and C-1222) and the Multidisciplinary University Research Initiative of the Army Research Office for their support.

Solvent-Free Electrolytes with Aqueous Solution–Like Conductivities

Wu Xu and C. Austen Angell*

Aqueous solutions are generally assumed to be superior electrolytic conductors because of the unique dielectric and fluid properties of water. We show that their conductivities can be matched by liquid electrolytes that contain no solvent. These are proton transfer salts that are liquid at ambient temperature. The high conductivities are due to the high fluidity and ionicity rather than some sort of Grotthus mechanism, although in certain cases a mobile proton population may make a non-negligible contribution. The highest conductivities have been obtained when both cations and anions contain protons. At 25°C, values of >150 millisiemens per centimeter (mS cm^{-1}) appear possible; at 100°C, 470 mS cm^{-1} has been measured. Because of the combination of high ionicity and proton exchange kinetics with low vapor pressure, the systems we describe also make excellent fuel cell electrolytes.

The study of electrical conductance in ionic solutions goes back to the earliest chapters of physical chemistry. It has been overwhelmingly the study of aqueous solutions. The concepts of ionic dissociation, and the battles fought to establish the reality of ions, were based on observations made on aqueous solutions (*1*). The more recent surge of interest in nonaqueous electrolyte systems (*2, 3*) has been driven, in part, by the quest for a rechargeable lithium battery. In this respect, the much lower conductivities characteristic of nonaqueous electrolytes have been a serious hurdle (*3*).

The ability of solutions to carry current, measured in S cm^{-1}, increases with increasing ion concentration from the low and often immeasurable values of the pure solvent. However, it always peaks at concentrations on the order of 1 M (versus $\sim$5 M for aqueous solutions) (*2*) because the electrostatic interaction between the ions of opposite charge, moderated by the dielectric constant of the solvent, causes a counterbalancing decrease in the individual ionic mobilities. For this reason, it is generally not expected that pure salts can be excellent conductors unless the temperature is raised to high values. We show that this expectation is not valid, and we identify conditions under which the conductivity of solvent-free ionic liquids (ILs) can be raised to aqueous solution levels.

ILs may be either protic or aprotic in nature. Protic ILs are formed by proton transfer between molecules that are, respectively, Brønsted acids and bases. Aprotic ILs are formed by transfer of an alkyl group (or a group of comparable complexity) to the same site occupied by a proton in a protic IL. The study of the aprotic ILs has become a major field focused on "green" chemistry (*4, 5*) but not limited to it (*6–11*).

We find that the fluidities and attendant conductivities of protic ILs tend to be much higher than those of aprotic ILs, for reasons that are not completely clear. Residual hydrogen bonding would suggest the opposite effect. The answer may lie in the reduction of the Madelung energy (the free energy reduction due to uniform distribution of negative around positive charge centers) that is responsible for the low vapor pressure of ILs and molten salts (*12–14*). Whatever the explanation, the higher fluidities lend protic ILs an important advantage in any application where protonation of more basic sites in the system is not a problem.

The possibility that fluidities of protic ILs could be exceptional became apparent to us during a study of glass transition temperatures (T_g) of ILs (*12*). T_g is where the liquid state begins: It is the temperature above which fluidity becomes measurable and is, of course, relevant to fluidity at room temperature. For ILs of comparable fragility [i.e., those in which the fluidity above T_g changes at the same rate with change of temperature (*15*)], the IL with the lower T_g will be the one that is more fluid at ambient temperature. The T_g values of simple mono- and disubstituted ammonium salts, obtained either directly or by short extrapolations of data on their mixtures, are found to be anomalously low. In

Department of Chemistry and Biochemistry, Arizona State University, Tempe, AZ 85287, USA.

*To whom correspondence should be addressed. E-mail: caa@asu.edu